

## Identification of carbon-containing phases in electrodeposited hard Fe–C coatings with intentionally codeposited carbon

Marcoen, Kristof; Gauvin, Mélanie; De Cleene, Ansbert; Obitsø Nielsen, Jacob; Baert, Kitty; Terryn, Herman; De Strycker, Joost; Hauffman, Tom; Pantleon, Karen

**DOI**

[10.1002/sia.7196](https://doi.org/10.1002/sia.7196)

**Publication date**

2023

**Document Version**

Final published version

**Published in**

Surface and Interface Analysis

**Citation (APA)**

Marcoen, K., Gauvin, M., De Cleene, A., Obitsø Nielsen, J., Baert, K., Terryn, H., De Strycker, J., Hauffman, T., & Pantleon, K. (2023). Identification of carbon-containing phases in electrodeposited hard Fe–C coatings with intentionally codeposited carbon. *Surface and Interface Analysis*, 55(5), 336-346.  
<https://doi.org/10.1002/sia.7196>

**Important note**

To cite this publication, please use the final published version (if applicable).  
Please check the document version above.

**Copyright**

Other than for strictly personal use, it is not permitted to download, forward or distribute the text or part of it, without the consent of the author(s) and/or copyright holder(s), unless the work is under an open content license such as Creative Commons.

**Takedown policy**

Please contact us and provide details if you believe this document breaches copyrights.  
We will remove access to the work immediately and investigate your claim.

***Green Open Access added to TU Delft Institutional Repository***

***'You share, we take care!' - Taverne project***

**<https://www.openaccess.nl/en/you-share-we-take-care>**

Otherwise as indicated in the copyright section: the publisher is the copyright holder of this work and the author uses the Dutch legislation to make this work public.

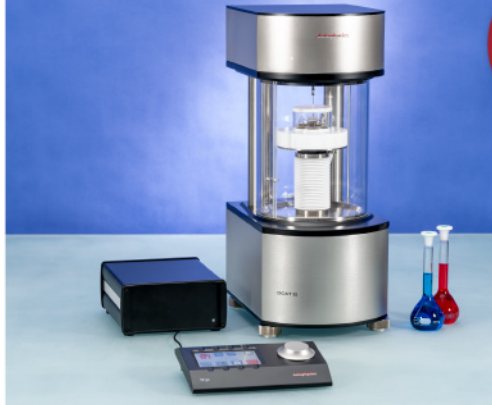


force tensiometry,  
dynamic contact angle  
measurements, and force  
of adhesion evaluation



ASTM D5946  
ASTM D7334  
ASTM D7490  
ISO 27448

optical contact angle  
measurements and  
drop contour analysis to  
determine surface energy  
as well as interfacial and  
surface tension



ASTM D1331  
ASTM D1417  
ISO 1409

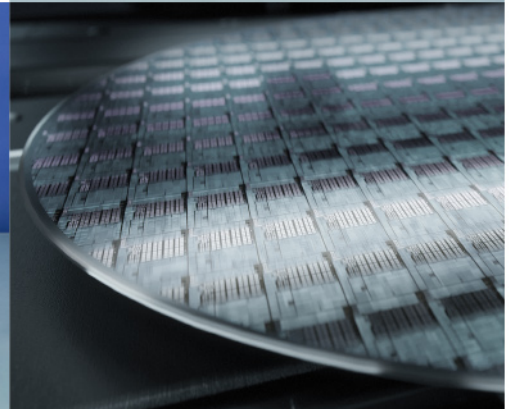


ISO/TR 13097

optical turbidity, stability  
and aging analysis of  
multi-phase dispersions



zeta potential  
measurements  
of fibres, powders, and  
plate-shaped solids



High-end, versatile laboratory  
measurement device portfolio  
for a comprehensive analysis of  
surfaces and interfaces


**Learn more >**

**dataphysics**  
Understanding Interfaces

DataPhysics Instruments GmbH  
Raiffeisenstraße 34 • 70794 Filderstadt, Germany  
phone +49 (0)711 770556-0 • fax +49 (0)711 770556-99  
sales@dataphysics-instruments.com  
www.dataphysics-instruments.com

## RESEARCH ARTICLE

# Identification of carbon-containing phases in electrodeposited hard Fe–C coatings with intentionally codeposited carbon

Kristof Marcoen<sup>1,2</sup>  | Mélanie Gauvin<sup>2</sup> | Ansbert De Cleene<sup>2</sup> |  
Jacob Obitsø Nielsen<sup>3,4</sup> | Kitty Baert<sup>1</sup> | Herman Terryn<sup>1,5</sup> | Joost De Strycker<sup>2</sup> |  
Tom Hauffman<sup>1</sup> | Karen Pantleon<sup>3</sup>

<sup>1</sup>Research Group of Electrochemical and Surface Engineering (SURF), Department Materials and Chemistry (MACH), Vrije Universiteit Brussel, Pleinlaan 2, Brussels, 1050, Belgium

<sup>2</sup>OCAS NV, President John F. Kennedylaan 3, Zelzate, 9060, Belgium

<sup>3</sup>Department of Civil and Mechanical Engineering, Technical University of Denmark, Produktionstorvet, Kongens Lyngby, 2800, Denmark

<sup>4</sup>Fiberline Composites, Middelfart, Denmark

<sup>5</sup>Department of Materials Science and Engineering, Delft University of Technology, Mekelweg 2, Delft, 2628 CD, The Netherlands

## Correspondence

Kristof Marcoen, Research Group of Electrochemical and Surface Engineering (SURF), Department Materials and Chemistry (MACH), Vrije Universiteit Brussel, Pleinlaan 2, 1050 Brussels, Belgium.  
Email: [kristof.marcoen@vub.be](mailto:kristof.marcoen@vub.be)

## Present address

Jacob Obitsø Nielsen, Department of Materials Science and Engineering, Delft University of Technology, Mekelweg 2, Delft, 2628 CD, The Netherlands.

## Funding information

Fonds Wetenschappelijk Onderzoek, Grant/Award Number: I006220N

Electrodeposition from an environmentally friendly iron sulfate electrolyte with citric acid as carbon source has gained attention recently, because of excellent mechanical properties of the resulting Fe–C coatings with intentionally codeposited high-carbon concentrations. While being very attractive as protective coatings and sustainable alternatives for hard chrome coatings, comprehensive understanding of the coatings' chemical constitution including the type and location of carbon-containing phases is still lacking. The amount of codeposited carbon of up to about 0.8 wt.% significantly exceeds the solubility of carbon in ferrite, although carbon-free ferrite is the only unambiguously reported phase in as-deposited Fe–C coatings so far. In the present work, time-of-flight secondary ion mass spectrometry, X-ray photoelectron spectroscopy, and soft X-ray emission spectroscopy have been applied to identify the carbon-containing phases, which are present as minor secondary phases in the coatings but are known to have an important influence on the coatings' properties. Three carbon-containing phases could be distinguished, homogeneously distributed in the nanocrystalline ferrite base material. Iron acetates, amorphous carbon, and carbides were found in both as-deposited and annealed Fe–C coatings up to 300°C, but their fraction changes during postdeposition annealing.

## KEYWORDS

annealing, carbon, chemical analysis, electrodeposition, Fe–C coating

## 1 | INTRODUCTION

The electrodeposition of iron-based coatings has a long tradition but, so far, is mainly applied owing to excellent magnetic properties of deposited iron alloys. Only recently, electrodeposition of iron alloys sparked new awareness as protective coatings. Driven by the urgent need for a sustainable, environmentally friendly alternative to hard chrome coatings, the ability to deposit particularly hard and wear resistant iron-based coatings has been demonstrated, and promising

mechanical properties are reported for the electrodeposition of iron–carbon coatings.<sup>1–7</sup> Despite the technological importance of iron–carbon bulk alloys (e.g., steels), the intentional codeposition of carbon from iron-based electrolytes has not gained much attention yet, and carbon in electrodeposited coatings is often either disregarded or called an impurity.<sup>8,9</sup> Typical electrolytes for electrodeposition of iron, for example, iron sulfate-based solutions, usually include citric acid or citrates, which are added primarily due to their role as complexing agents, as buffers, or to enhance the electrolyte stability. The applied

electrolytes are free of any other additives like dedicated levelers or brighteners; thus, the sole presence of citric acid, which is naturally occurring and hazard free, allows for environmentally friendly electrodeposition without harmful substances. In these electrolytes, obviously, the citric acid provides the source of carbon and facilitates its codeposition. The successful intentional codeposition of carbon with high concentrations of about 0.8 wt.% C results in excellent mechanical properties (e.g., hardness of about 800 HV for as-deposited coatings and up to 1300 HV after annealing)<sup>2-4,6,10,11</sup> and suggests an enormous potential for surface engineering using iron-carbon coatings. The coatings can be deposited reproducibly with high-carbon concentrations of homogeneous distribution within coating thicknesses of up to several hundreds of micrometers. Owing to good ability for surface leveling and good adhesion to subsequently deposited multilayers,<sup>7</sup> the electrodeposition of iron-carbon coatings can be applied either for local repair of damaged surfaces or as continuous coatings whenever surface protection from mechanical attack is needed (e.g., as work rolls for cold rolling mills). Albeit the reproducible electrodeposition and well-defined properties of iron-carbon coatings are very attractive for industrial applications, a comprehensive understanding of the coatings' chemical constitution including the type and location of carbon-containing phases has not been obtained yet.

One of the challenges in understanding the codeposition of carbon and the resulting formation of carbon-containing phases relates to the difficulties of straightforward experimental characterization of as-deposited coatings. In thermodynamic equilibrium, carbon is almost insoluble in the bcc  $\alpha$ -iron lattice (ferrite). Indeed, carbon-free ferrite is revealed by diffraction analysis for as-deposited coatings.<sup>2,3,6</sup> In addition to ferrite, the presence of one additional diffraction peak is reported consistently<sup>2-6</sup> and indicates the presence of (at least) one more crystalline phase in the as-deposited coatings. However, an unambiguous phase identification is not possible by diffraction analysis and, accordingly, a yet "nameless" phase has been proposed in addition to the identified ferrite.<sup>4-6</sup> Although it is likely that it contains carbon, the so far reported results cannot explain the measured high-carbon concentrations of about 0.8 wt.% C, and partly inconsistent explanations are proposed in the need to locate the high-carbon content in the coatings.<sup>2,4,5,10-12</sup> Together with the codeposition of carbon, also hydrogen and oxygen are frequently detected in as-deposited iron-carbon coatings,<sup>3-5,11-14</sup> although often ignored as impurities or related to unwanted side effects. The abovementioned difficulties of identifying the intentionally codeposited carbon in the coatings are further complicated by the simultaneous presence of oxygen and hydrogen, which provide various possibilities for the formation of crystalline and noncrystalline phases during electrodeposition and affect their evolution during postdeposition annealing.

The importance of all the codeposited elements (C, O, and H) for mechanical properties is documented in previous studies both for as-deposited and postdeposition annealed iron-carbon coatings.<sup>3-6</sup> The chemical and phase constitution resulting from the codeposited elements (C, O, and H), which has not yet been possible to reveal, is addressed with the present work. Using labeled isotopes in the

electrolyte and by means of complementary spectroscopic methods, the origin and type of phases in both as-deposited and annealed iron-carbon coatings is investigated. Techniques that were used are time-of-flight secondary ion mass spectrometry (ToF-SIMS), X-ray photoelectron spectroscopy (XPS), Raman spectroscopy, and soft X-ray emission spectroscopy (SXES).

## 2 | MATERIAL AND METHODS

### 2.1 | Coatings

Electrochemical deposition of iron-carbon (Fe-C) coatings occurred from a 100 mL iron sulfate electrolyte with citric acid as carbon source: 80 g/L of iron(II) sulfate heptahydrate ( $\text{FeSO}_4 \cdot 7\text{H}_2\text{O}$ ) and 1.2 g/L of citric acid ( $\text{C}_6\text{H}_8\text{O}_7$ —Merck). The pH of the electrolyte is adjusted to pH 2.5 by sulfuric acid. The applied electrolyte and process parameters correspond to previous studies that optimized the coating process.<sup>3</sup>

For unambiguous identification of the codeposited carbon in the coatings by ToF-SIMS, a second batch of electrolyte was prepared in a similar way with isotopic citric acid ( $^{13}\text{C}_6\text{H}_8\text{O}_7$ , Sigma Aldrich), where all  $^{12}\text{C}$  are replaced with  $^{13}\text{C}$ . The obtained coatings are referred to as Fe- $^{13}\text{C}$  coatings in comparison to the Fe- $^{12}\text{C}$  coatings.

The Fe-C coatings were electrodeposited on a cold rolled low carbon steel grade DC06 as substrate. The steel composition as shown in Table 1 was determined using SS-OES and combustion analysis by Leco CS600 (C and S) and Bruker Galileo G8 (N and O).

The substrate was submitted to a cleaning procedure prior to the electrodeposition process. The cleaning procedure consisted of an ultrasonic solvent cleaning in Dowlene™ 1601 (propyleneglycol-*tert*-butylether) followed by anodic electrolytic cleaning in ENPREP OC (MacDermid-Enthone) for 1 min at 15 A/dm<sup>2</sup> and 45°C and subsequent double rinsing steps in deionized water. An oxide removal step prior to immersion in the electrodeposition electrolyte was performed in 10 V/V% sulfuric acid solution for 1 min at room temperature followed by rinse with deionized water. The electrodeposition process was carried out in a double-walled thermostat beaker at 50°C. The specimens were deposited on both sides of the DC06 steel substrate sheets using parallel faced anodes also made from DC06 steel. A current density of 3.5 A/dm<sup>2</sup> was applied for 60 min to obtain a targeted 45  $\mu\text{m}$  coating thickness.

After coating, the samples are rinsed with deionized water and dried with compressed air. To avoid further contamination with time, the specimens are packed in Al foil.

### 2.2 | Thermal annealing

In addition to as-deposited coatings, also coatings after annealing were investigated. To this end, isothermal annealing was carried out at various temperatures (150°C, 240°C, 300°C, 400°C, and 600°C) for different durations in an Argon atmosphere in a TGA equipment

**TABLE 1** Composition of the steel substrate in wt.% (the balance corresponds to iron).

| C      | O      | S      | N      | Mn     | Al     | Ti     |
|--------|--------|--------|--------|--------|--------|--------|
| 0.0025 | 0.0046 | 0.0090 | 0.0019 | 0.1230 | 0.0430 | 0.0560 |

Q500 from TA instruments. Round specimens were cut from the larger electrodeposited area and placed in a platinum pan. The system was purged with Argon (>99.9999% purity, balance 40 mL/min, sample 60 mL/min). The annealing temperature and duration are summarized in Table 2.

After annealing at 400°C and 600°C for 3 h, the specimens showed visible cracking and oxidation.

## 2.3 | ToF-SIMS

To obtain molecular information and to detect fragments and elements with high sensitivity (ppm–ppb range), ToF-SIMS was used. ToF-SIMS measurements were performed with a TOF.SIMS 5 system from ION-TOF GmbH (Münster, Germany), using a 30 keV Bi<sub>3</sub><sup>+</sup> primary ion beam operated in the high-current bunched mode for high mass resolution (approximately 8000 at 29 u [<sup>29</sup>Si<sup>+</sup>]). ToF-SIMS is a surface sensitive technique with an analysis depth of 1–5 nm. The lateral resolution achieved in the high-current bunched mode is 3 µm. The pulsed ion beam target current was approximately 0.70 pA. Positive and negative ion mass spectra were acquired over a mass range of 1–800 u. Depth profiles were obtained in dual beam configuration, where a 20 keV Ar<sub>1200</sub><sup>+</sup> cluster ion beam was used as a sputter beam, and Bi<sub>3</sub><sup>+</sup> was used to analyze the crater bottom. Positive polarity spectra are obtained by applying a negative extractor voltage, and negative polarity spectra are obtained by applying a positive extractor voltage. The sputter raster was set to 800 µm × 800 µm, and the sputter ion fluence was  $1.20 \times 10^{14}$  ions cm<sup>-2</sup> s<sup>-1</sup>. A smaller analysis raster of 100 µm × 100 µm was chosen in the center of the crater.

A VLS-80 system (Nanoscan, Zürich, Switzerland) integrated in the TOF.SIMS 5 system was used to obtain sputter depth information. An atomic force microscopy (AFM) surface profile (long-distance line scan) was obtained across the sputter crater and compared with a reference line scan obtained before sputtering. This allows to determine the shape and depth of the crater. Measurements were done in contact mode with a diamond-coated NANOSENSORS DT-CONTR AFM probe. The probe tip height is between 10 and 15 µm, and the tip radius (at the narrow end of the tip) is in the 10 nm regime.

## 2.4 | XPS

XPS was performed using a VersaProbe III photoelectron spectrometer from PHI. All spectra were collected using monochromatic Al Kα X-rays (1486.6 eV) operating at 300 W. High-resolution spectra were obtained using a pass energy of 23.5 and 0.1 eV energy step size. The spot size was 100 µm, and the take-off angle between the X-rays and

**TABLE 2** Thermal annealing parameters.

|          | T (°C) |     |     |     |     |
|----------|--------|-----|-----|-----|-----|
|          | 150    | 240 | 300 | 400 | 600 |
| Time (h) | 6      | 12  | 3   | 3   | 3   |

spectrometer was 45°. Fitting of the peaks was done with CasaXPS software using a Shirley background and a mixed Gaussian–Lorentzian shape. All the spectra were calibrated with respect to the C–C/C–H contribution in the C1s signal fixed at 284.8 eV.

## 2.5 | Raman spectroscopy

The samples were analyzed with a LabRAM HR Evolution confocal Raman spectroscope from Horiba Scientific in an attempt to accurately identify the sp<sup>2</sup>/sp<sup>3</sup> carbon ratio in the coatings. The green laser (532 nm) was employed with 10% filter and 100× objective for optical images and Raman measurements. The data were analyzed with the standard LabSpec 6.2 software, including spike removal and background correction.

## 2.6 | SXES

SXES is a spectroscopic technique that gives information about the partial density of state of the valence bands of atoms with a high energy resolution comparable to XPS and Auger spectroscopies.<sup>15,16</sup> SXES is used to quantify concentrations of light elements and probe their chemical state through their characteristic peak position and shape. While XPS and ToF-SIMS provide surface chemical information within 1 to 10 nm in depth, the depth of analysis of SXES is in the range of several hundreds of nanometers, in an iron matrix at 5 kV. Thus, SXES provides average elemental and chemical state information over a larger range of depth. Samples were subjected to chemical analysis with a JEOL SS-94000 detector attached to a scanning electron microscope JEOL 8530F FEG-EPMA. A 5 kV acceleration voltage, 200 nA probe current, and 60 s accumulation time were used. SXES spot measurements were performed over a 10 × 10 grid with a 10 µm step size and 1 µm beam diameter. For each sample, 100 spectra were collected and averaged to improve the signal-to-noise ratio of the measurements. The energy resolution of the SXES detector is 0.2 eV and was calibrated at the edge of Al–K line at 72.5 eV. SXES peaks were identified using the indexing-tool provided with the SXES software from JEOL. The net intensities of the carbon peak (C–Kα at 138.6 eV) and oxygen peak (O–Kα at 174.7 eV) are converted to

concentrations using the calibration line method with reference materials of steels and iron oxide with known C content and O content, respectively. The SXES spectra of bulk graphite and a gold-coated pellet of sodium acetate trihydrate (analytical grade) were measured under the same beam current, acceleration voltage, and accumulation time conditions as the coatings.

### 3 | RESULTS

#### 3.1 | Identification of the carbon phase in as-deposited coatings

Carbon being codeposited in the coating must originate from the citric acid in the electrolyte. In order to verify the nature of carbon and confirm its origin, coatings were prepared from an electrolyte that contained isotopic citric acid in which all  $^{12}\text{C}$  are replaced by  $^{13}\text{C}$ . ToF-SIMS offers isotopic discrimination, which enables to distinguish the carbon codeposited during the electrochemical process from carbon contamination. To avoid the top-surface contamination, the coating was sputtered using a 20 keV  $\text{Ar}_{1200}^+$  sputter ion source prior to analysis.

Figure 1A shows the negative polarity spectrum obtained from the  $\text{Fe}-^{13}\text{C}$  coating at a depth of 260 nm.  $\text{FeO}_2^-$  and  $\text{Fe}_2\text{O}_3^-$  are much lower in intensity as compared with the top-surface spectrum (Figure S1a).  $\text{Fe}_x\text{O}_y^-$  fragments (with  $x = y$ ) became more prominent, and even  $\text{Fe}_x\text{O}_y^-$  fragments (with  $x > y$ ) and  $\text{Fe}_x^-$  fragments are now observed. Furthermore, the detection of  $^{13}\text{C}^-$  and  $^{13}\text{C}_2^-$  indicates the presence of a carbon phase in the coating that originates from the citric acid in the electrolyte. Figure 1B shows the ToF-SIMS spectra obtained in positive polarity. The spectrum at a depth of 260 nm is dominated by  $\text{Fe}_x^+$  fragments (Figure 1B), unlike the top-surface spectrum which is dominated by  $\text{Fe}_x\text{O}_y^+$  fragments (Figure S1b). This indicates that iron in the coating is present in highly reduced form and this corresponds to earlier investigations in literature, which identified the main crystalline phase in the as-deposited iron-carbon coating as ferrite.<sup>3,5</sup>

The present study is focused on identification of the carbon phase in the electrodeposits. Figure 1 shows  $^{13}\text{C}^-$  and  $^{13}\text{C}_2^-$  as the

most intense carbon fragments. Additional carbon fragments can be found by further zooming in on the spectra. Figure 2 shows an overview of the most prominent  $^{13}\text{C}$  containing fragments that were found in the  $\text{Fe}-^{13}\text{C}$  coating (blue spectra). Spectra obtained for the regular  $\text{Fe}-^{12}\text{C}$  coating (in orange) are shown in overlay to confirm the identification of  $^{13}\text{C}$  containing fragments.

Assignments of carbon-containing fragments can be divided into three categories. Figure 2A shows  $\text{Fe}_x^{13}\text{C}^+$  fragments, which indicate the presence of an iron carbide phase. Figure 2B shows  $^{13}\text{C}_2\text{H}_3\text{O}_2^-$ , a fragment attributed to an organic phase that must be closely related to citric acid ( $^{13}\text{C}_6\text{H}_8\text{O}_7$ ).  $^{13}\text{C}_2\text{H}_3\text{O}_2^-$  corresponds to an acetate structure. Fragment  $^{13}\text{C}_2\text{HO}_2\text{Fe}^-$  and especially fragment  $^{13}\text{C}_2\text{H}_3\text{O}_3\text{Fe}^-$  suggest that iron acetate complexes are present in the coatings. Figure 2C shows distinct mass peaks for  $^{13}\text{C}_2^-$ ,  $^{13}\text{C}_3^-$ ,  $^{13}\text{C}_4^-$ ,  $^{13}\text{C}_2\text{H}^-$ , and  $^{13}\text{C}_4\text{H}^-$ . This series of  $^{13}\text{C}_x(\text{H}_y)^-$  fragments seems to correspond to a third carbon-containing phase.

XPS analysis is performed in addition to ToF-SIMS to aid in the identification of the carbon-containing phases. Figure 3 shows C1s high-resolution spectra obtained on the  $\text{Fe}-^{13}\text{C}$  coating and elemental compositions deduced from the accompanying survey spectra. Figure 3A shows a spectrum obtained at the top surface. From ToF-SIMS (Figure S1), it is known that no carbon related to the electrodeposition process is present at the oxidized and contaminated top surface with about 10 nm thickness; therefore, this spectrum can be regarded as a carbon contamination spectrum. Figure 3B shows a spectrum obtained at a depth of 260 nm in a crater that had been created earlier for ToF-SIMS analysis. C1s spectra are peak fitted and calibrated with respect to the C-C/C-H component which is fixed at 284.8 eV. Table 3 gives an overview of C1s components used in peak fitting. The C1s spectrum obtained at 260 nm depth (Figure 3B) resembles strongly the spectrum obtained at the top surface (Figure 3A). One remarkable difference is that an additional peak at binding energy 282.7 eV is observed in Figure 3B. This shift in binding energy ( $-2.1$  eV with respect to C-C/C-H) indicates the presence of a carbide phase.<sup>11,17</sup> The carbon signal in Figure 3B corresponds to a carbon content of 4.7 wt.%, which strongly exceeds the average carbon content (0.6–1.2 wt.%) reported for electrodeposited Fe-C coatings.<sup>1–3,11–13</sup> The high-carbon content and the strong resemblance with the spectrum in Figure 3A allows to conclude that also Figure 3B

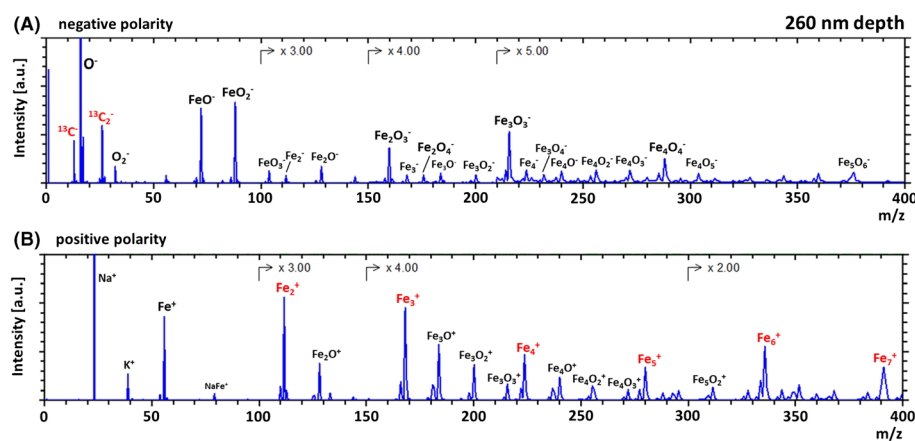


**FIGURE 1** ToF-SIMS spectra (0–400  $m/z$ ) obtained in (A) negative and (B) positive polarity from the  $\text{Fe}-^{13}\text{C}$  coating. Analysis was performed at 260 nm depth (crater created with a 20 keV  $\text{Ar}_{1200}^+$  sputter source).

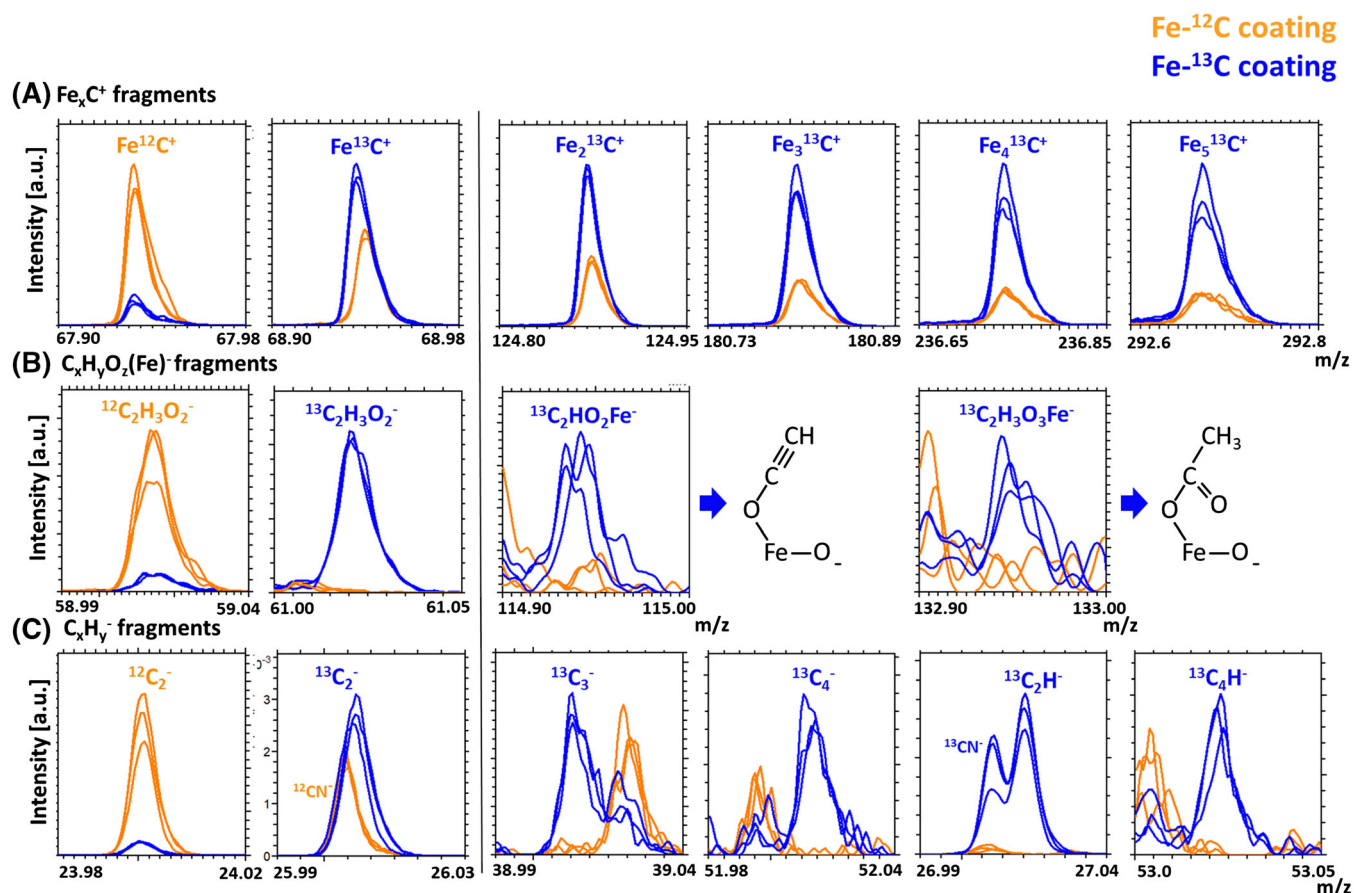
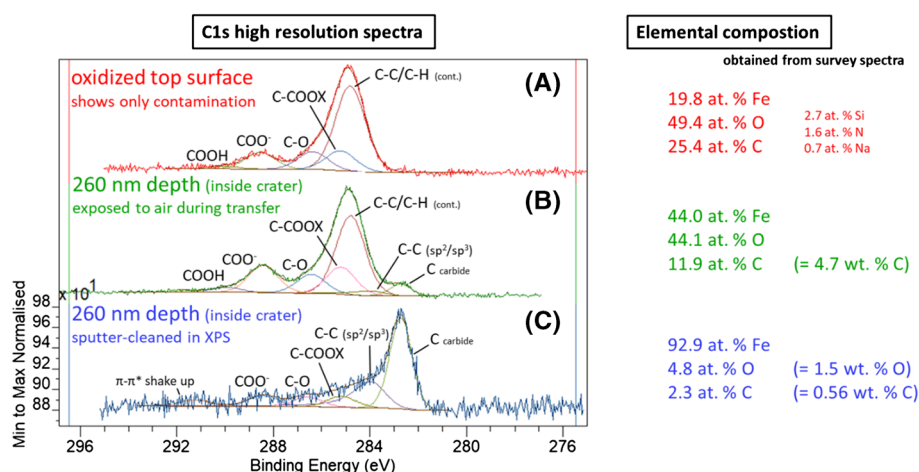


**FIGURE 2** Carbon-containing fragments identified in the ToF-SIMS spectra for a Fe-<sup>13</sup>C coating (blue) and for a Fe-<sup>12</sup>C coating (orange). Each figure shows an overlay of three spectra per sample. Fragments are divided in three categories: (A) Fe<sub>x</sub>C<sup>+</sup> fragments. (B) C<sub>x</sub>H<sub>y</sub>O<sub>z</sub>(Fe)<sup>-</sup> fragments. (C) C<sub>x</sub>H<sub>y</sub><sup>-</sup> fragments.

**FIGURE 3** Left: Carbon 1s XPS spectra (minimum to maximum normalized) after curve fitting. (A) Oxidized top surface. (B) Inside crater generated earlier for ToF-SIMS analysis at 260 nm depth. (C) Inside crater generated earlier for ToF-SIMS analysis at 260 nm depth. The crater was sputter cleaned in XPS with an Ar gas cluster ion beam. Right: Corresponding elemental composition obtained from accompanying survey spectrum.



is dominated by carbon contamination. In addition, Fe2p high-resolution spectra show that iron is mainly present in oxidized form (Figure S2). Both the presence of carbonaceous contamination and oxidation of iron can be explained by the fact that the sample has been exposed to air during transfer from ToF-SIMS analysis to XPS analysis. Figure 3C shows a spectrum obtained in the same crater (at 260 nm depth) after sputter cleaning with an Ar gas cluster ion

beam (20 keV Ar<sub>2500</sub><sup>+</sup>). The carbide peak is now dominating the spectrum. An additional component is clearly observed at binding energy 284.0 eV (−0.8 eV with respect to C-C/C-H). This binding energy, together with a π-π\* shake-up peak observed at 291.3 eV, is indicative for a sp<sup>2</sup> carbon phase.<sup>17–19</sup> The presence of an amorphous carbon phase can account for the C<sub>x</sub><sup>-</sup> fragments that are observed in ToF-SIMS. Due to small differences in binding energy for sp<sup>2</sup> and sp<sup>3</sup>

**TABLE 3** Peak assignments for the C1s components used in curve fitting

| Assignment                              | Binding energy (eV) | FWHM (eV) |
|---|---------------------|-----------|
| C-Fe (carbide)                          | 282.7               | 1.0       |
| C-C (sp <sup>2</sup> /sp <sup>3</sup> ) | 284.0               | 1.4       |
| C-C/C-H                                 | 284.8               | 1.4       |
| C-COO <sup>-</sup>                      | 285.2               | 1.4       |
| C-O                                     | 286.6               | 1.4       |
| COO <sup>-</sup>                        | 288.4               | 1.4       |
| π-π* shake-up                           | 291.3               | 1.4       |

components, it is not possible for amorphous carbon to fully separate the sp<sup>2</sup> and sp<sup>3</sup> components in C1s XPS peak fitting.<sup>19</sup> Therefore, the component at binding energy 284.0 eV will be denoted as C-C (sp<sup>2</sup>/sp<sup>3</sup>).

Finally, a small peak at binding energy 288.4 eV (+3.6 eV with respect to C-C/C-H) can be attributed to COO<sup>-</sup>.<sup>20</sup> The presence of carboxylate groups after sputter cleaning corresponds well with the organic fragments that were picked up by ToF-SIMS.

Results from the XPS analysis are in line with those from ToF-SIMS analysis on the same samples. The results indicate that not one, but three carbon phases are present in the as-deposited coating: a carbide phase, a carbon phase with sp<sup>2</sup> (and maybe less sp<sup>3</sup>) bonding, and an acetate phase. The sp<sup>2</sup>/sp<sup>3</sup> ratio of a carbon phase is difficult to determine with XPS,<sup>21</sup> especially when three different carbon phases are present in very low concentration. An attempt was made to characterize the amorphous carbon phase with Raman spectroscopy (Figure S3). Unfortunately, no peak related to a carbon phase was found. It is likely that the concentration of this carbon phase is too low to be detected by Raman spectroscopy. XPS points to amorphous carbon in form of the trigonal a-C phase with predominantly sp<sup>2</sup> bonding rather than the tetrahedral amorphous carbon (ta-C) phase.<sup>22</sup> A hydrogenated amorphous carbon (a-C:H) phase cannot be excluded, because we find <sup>13</sup>C<sub>2</sub>H<sup>-</sup>, and <sup>13</sup>C<sub>4</sub>H<sup>-</sup> fragments in the ToF-SIMS spectra (Figure 2).

## 3.2 | Influence of annealing on the chemical composition

### 3.2.1 | ToF-SIMS depth profiles

Fe-C coatings were subjected to isothermal annealing. ToF-SIMS depth profiles were acquired on an as-deposited Fe-<sup>13</sup>C coating (Figure 4A) and on Fe-<sup>13</sup>C coatings annealed at temperatures up to 300°C (Figure 4B-D). Fe<sub>x</sub>O<sub>y</sub><sup>-</sup> (x < y) fragments are representative for an iron oxide phase. Each coating is characterized by an oxidized top layer. For the as-deposited coating and the coating annealed at 150°C, the oxidized top layer is estimated to be only about 10 nm thin and can be considered a native oxide that forms unrelated to annealing. At higher annealing temperatures, a thermal oxide layer is formed.

This thermal oxide layer grows in thickness with temperature, starting from 70 nm in the 240°C annealed coating to 200 nm in the 300°C annealed coating. All depth information is derived from AFM line scans obtained across the sputter craters (Figure S4).

Beneath the native oxide or thermal oxide, similar results are revealed by ToF-SIMS for all samples. Spectra are dominated by Fe<sub>x</sub><sup>-</sup> and Fe<sub>x</sub>O<sub>y</sub><sup>-</sup> (with x > y) fragments, which illustrates the reduced nature of iron in the coating. Organic acetate (represented by <sup>13</sup>C<sub>2</sub>H<sub>3</sub>O<sub>2</sub><sup>-</sup>), iron carbide (represented by <sup>13</sup>CFe<sup>-</sup>), and sp<sup>2</sup> carbon (represented by <sup>13</sup>C<sub>2</sub><sup>-</sup>, <sup>13</sup>C<sub>3</sub><sup>-</sup>, and <sup>13</sup>C<sub>4</sub><sup>-</sup>) phases are simultaneously present throughout the coating. This suggests that all carbon phases are well dispersed in the nanocrystalline coating.

### 3.2.2 | Evolution of carbon phases by SXES

SXES was performed on an as-deposited Fe-C coating and on Fe-C coatings annealed at temperatures up to 300°C. The SXES analyses were localized inside the craters created by Ar-cluster sputtering during the ToF-SIMS experiment. The SXES spectra of the as-deposited Fe-<sup>12</sup>C and Fe-<sup>13</sup>C coatings are both successfully indexed as Fe, C, and O soft X-ray emission lines, as shown in Figure 5 where the most intense Fe, C, and O peaks are labeled. Note that the peak labeling refers to the element, the type of X-ray line, and the reflection order in parenthesis. Figure 5 shows that SXES spectra of the as-deposited Fe-<sup>12</sup>C and Fe-<sup>13</sup>C coatings are qualitatively similar; thus, only the Fe-<sup>12</sup>C coatings (as-deposited and annealed) will be reported below. The complete set of Fe, C, and O X-ray emission lines with all reflection orders of the as-deposited coating are reported in Figure S5 and Table S1.

The effect of annealing on the coating's chemical composition is assessed through variations of the most intense SXES peaks for C, O, and Fe. Figure 6A-C shows detailed SXES C- (Kα [2] at 138.6 eV), O- (Kα [3] at 174.7 eV), and Fe- (LL [3] at 205.4 eV) peaks from the as-deposited and annealed coatings up to 300°C. For the investigated coatings, the C-peak intensity decreases with increasing annealing temperature, while the peak intensities of oxygen and iron remain almost unaffected by annealing. After annealing at both 150°C and 240°C, the position at maximum intensity of the C-Kα peak and the corresponding full-width-half-maximum (FWHM) values of the annealed coatings are identical to that of the as-deposited one, indicating good thermal stability in this temperature range. In contrast, at 300°C, these spectral features change suddenly. Indeed, the maximum of the C-Kα peak is shifted toward higher energy (138.6 eV for the as-deposited state vs. 139.0 eV after 300°C annealing) and the FWHM value is reduced from 4.1 to 3.4 eV by annealing at 300°C. The strong spectral variations of the C-Kα peak indicate a phase transformation that involves mostly carbon atoms and occurs due to annealing at 300°C.

From ToF-SIMS and XPS analysis, three chemically distinct carbon-based phases are suggested in the as-deposited and annealed coatings up to 300°C: a sp<sup>2</sup> carbon phase, an organic phase in the form of acetate, and an inorganic phase in the form of carbides. To

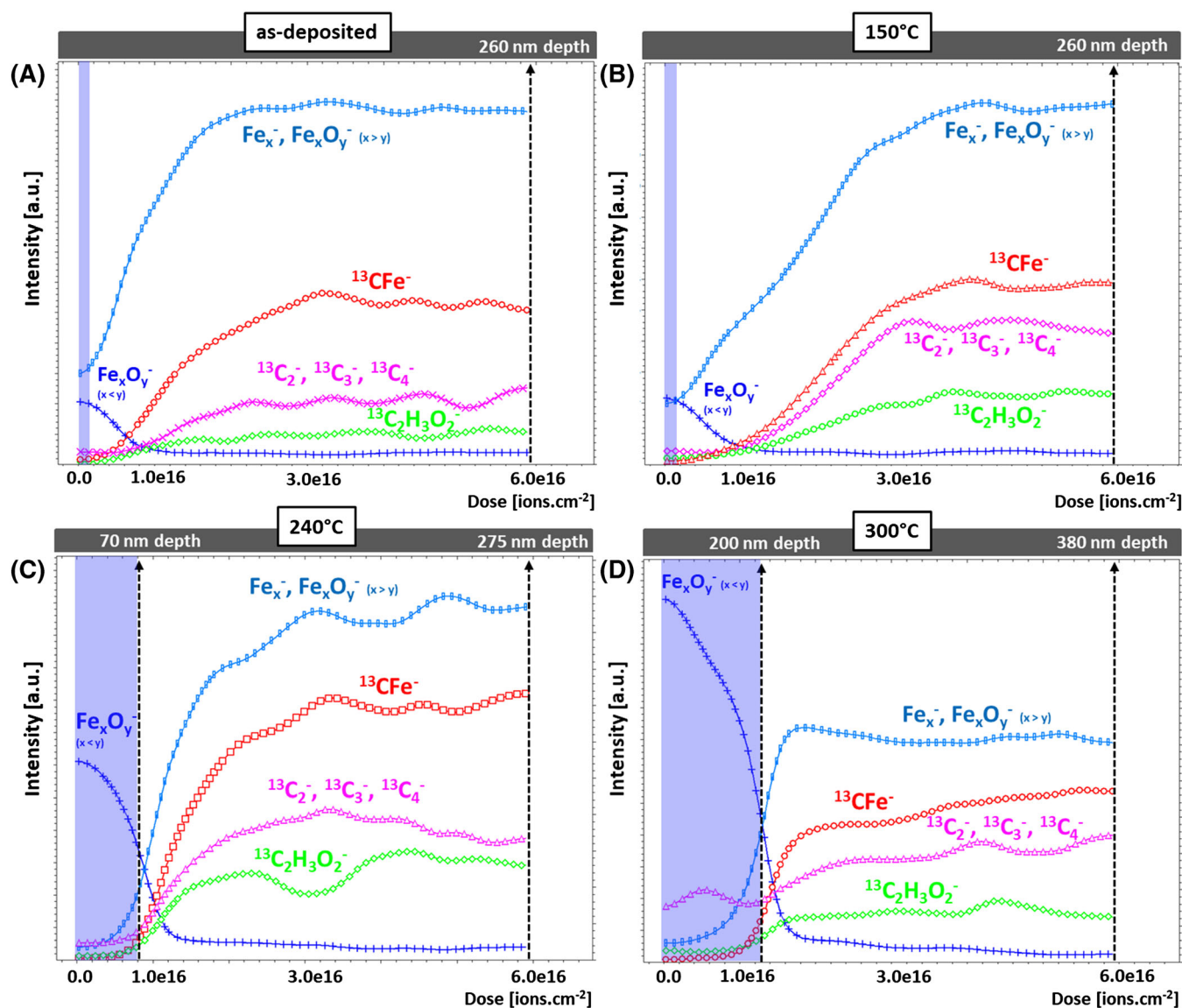


**FIGURE 4** ToF-SIMS depth profiles obtained with a 20 keV  $\text{Ar}_{1200}^{+}$  sputter source for (A) the as-deposited Fe- $^{13}\text{C}$  coating and for the Fe- $^{13}\text{C}$  coatings annealed at (B) 150°C, (C) 240°C, and (D) 300°C. Depths shown in the profiles are derived from AFM line scans across the sputter craters (Figure S4). Native iron oxide layers (for as-deposited and 150°C) and thermal iron oxide layers (for 240°C and 300°C) are shaded in blue.

confirm the coexistence of both organic and inorganic C-based phases in the coatings, the SXES spectra of graphite, sodium acetate trihydrate and of carbide-containing steel (0.82 wt.% C) were measured and compared with the as-deposited coating and coating annealed at 300°C, as shown in Figure 7.

In Figure 7A, the C-K $\alpha$  peak of the coating after annealing at 300°C is shifted by 0.4 eV toward higher energy and the FWHM value is reduced by 0.7 eV as compared with the C-K $\alpha$  peak of the as-deposited coating. Differences in C-K $\alpha$  peak position (indicated by dotted lines) and FWHM values are larger than the SXES detector energy resolution of 0.2 eV. Note that in Figure 7, intensities are normalized and do not reflect the relative amount of carbon inside the different samples.

Figure 7B,C compares the measured C-K $\alpha$  peaks of the as-deposited and the 300°C annealed coatings with the ones for reference samples. Acetate shows a maximum intensity at 138.6 eV and a FWHM value of 3.8 eV, while the C-K $\alpha$  peak of graphite is located at 138.2 eV with a FWHM value of 3.4 eV. The C-K $\alpha$  peak of carbide-containing steel is clearly distinct from that of acetate and graphite with peak position at 139.0 eV and FWHM value of 2.0 eV.

The similarity of C-K $\alpha$  peaks measured for both the as-deposited Fe-C coating and the acetate reference sample (see Figure 7B) with respect to the position of maximum peak intensity and FWHM values suggest that acetate is the dominant carbon phase in the as-deposited Fe-C coating. This seems contradictory to XPS, where the carbide

phase was the dominant carbon phase and thus suggests that the concentration of the acetate phase in the XPS spectrum is an underestimation of the actual concentration in the coating. An explanation lies in the different sensitivity of both techniques and in the organic acetate phase being most affected by the sputtering process. SXES is less affected by sputtering damage effects; the analysis depth with SXES

is in the range of several hundreds of nanometers, while the analysis depth in XPS only goes up to 10 nm.

It is likely that acetate coexists with  $sp^2$  carbon and carbide phases in the as-deposited Fe-C coatings, as shown by ToF-SIMS and XPS. The broad C-K $\alpha$  peak results from the convolution of a strong acetate C-K $\alpha$  peak with less intense contributions related to  $sp^2$  carbon and carbides, which are difficult to distinguish in a broad peak shape with large FWHM value. Upon annealing at 300°C, the C-K $\alpha$  peak shift and reduced FWHM value suggest that the carbide fraction has increased at the expense of the organic carbon in the Fe-C coating annealed at 300°C. Likely, this indicates the decomposition of the iron acetate fraction in Fe-C coatings, which is reported to start just below 300°C and is accompanied by the release of CO<sub>2</sub>.<sup>23,24</sup>

Figure 8 shows the C and O concentration in the as-deposited and annealed coatings up to 300°C. The as-deposited coating contains  $0.6 \pm 0.1$  wt.% of carbon and 2.5 wt.% of oxygen. The carbon concentration as determined by SXES is in good agreement with values found in XPS. The oxygen concentration in SXES shows larger values than the 1.5 wt.% of oxygen found using XPS. This small difference could be explained by a native oxide layer that forms within 1 day after the sample is removed from the vacuum environment in ToF-SIMS or XPS. The C concentration decreases to  $0.4 \pm 0.1$  wt.% after annealing at 300°C. Meanwhile, the O concentration remains stable with annealing up to 300°C. The loss of carbon associated with the strong variation in the C-K $\alpha$  peak (see Figure 6A) suggest that the organic carbon fraction is decreased upon annealing at 300°C.

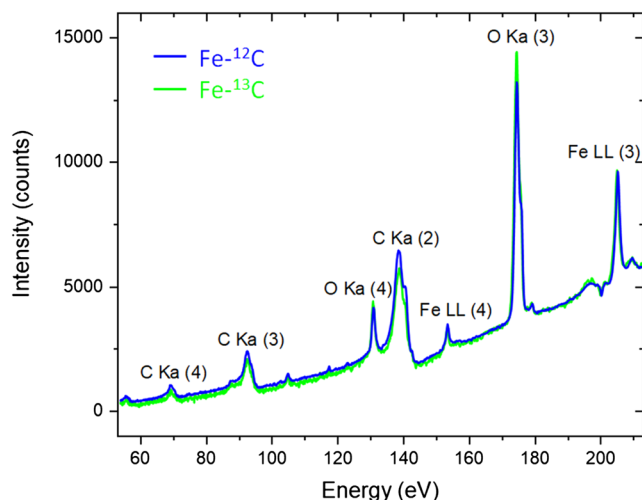


**FIGURE 5** SXES spectra of the as-deposited Fe-<sup>12</sup>C and Fe-<sup>13</sup>C coatings. The most intense peaks are labeled with their element, X-ray line, and corresponding (harmonic) order in parenthesis.

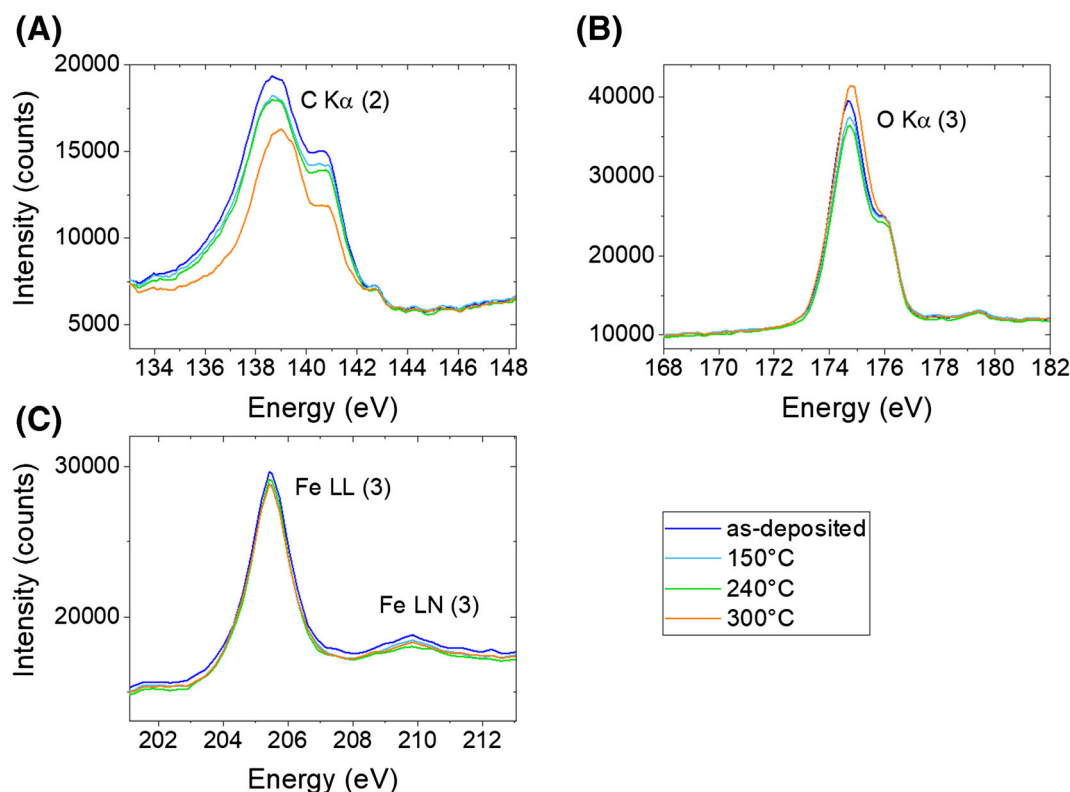


**FIGURE 6** Evolution of (A) C-K $\alpha$ , (B) O-K $\alpha$ , and (C) Fe-LL X-ray emission lines of iron-carbon coatings as a function of annealing temperature revealed by SXES.

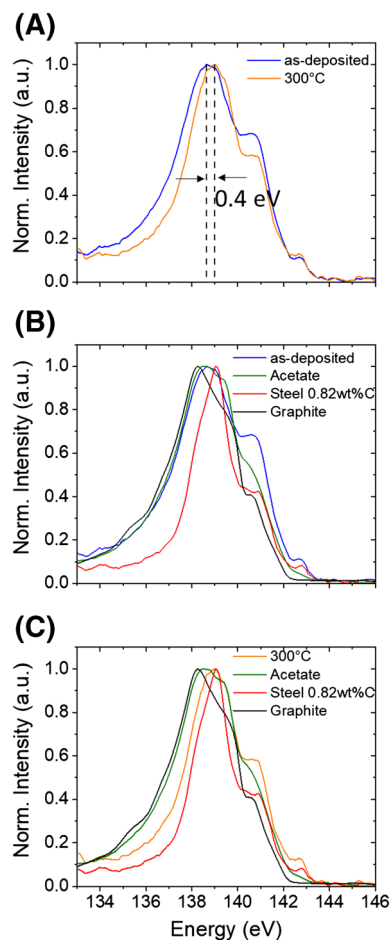


**FIGURE 7** SXES spectra. (A) Comparison of the C-K $\alpha$  peaks measured for the as-deposited coating and after annealing at 300°C. (B) Comparison of the C-K $\alpha$  peaks measured for the as-deposited coating, acetate, high-carbon steel (0.82 wt.% carbon) and graphite that serve as reference spectra. (C) Comparison of the C-K $\alpha$  peaks measured for 300°C annealed coating, acetate, high-carbon steel (0.82 wt.% carbon), and graphite that serve as reference spectra. Note that intensities are normalized.

## 4 | DISCUSSION

The various spectroscopic methods applied in the present work (ToF-SIMS, XPS, SXES, and Raman spectroscopy) essentially enhance the understanding of electrodeposited Fe-C coatings, which previously posed challenges in identifying the carbon-associated phases.<sup>2–6,10,12</sup> At first view, the measured high-carbon concentrations (0.6–1.2 wt.%) in electrodeposited Fe-C coatings,<sup>1,2,4,10,12</sup> being as high as in bulk Fe-C alloys (steels), suggest that carbon is present alike in steels, that is, in either supersaturated solid solution and/or in carbides, which typically could be revealed by diffraction analysis. Biased attempts in literature of interpreting diffraction results toward the classical understanding of unalloyed steels do not withstand closer inspection<sup>5</sup> and rather indicate that other mechanisms apply for the interplay between iron and carbon in case of electrodeposition. Elucidating the carbon-containing phases in Fe-C electrodeposits requires dedicated chemical and phase analysis as applied in the present work.

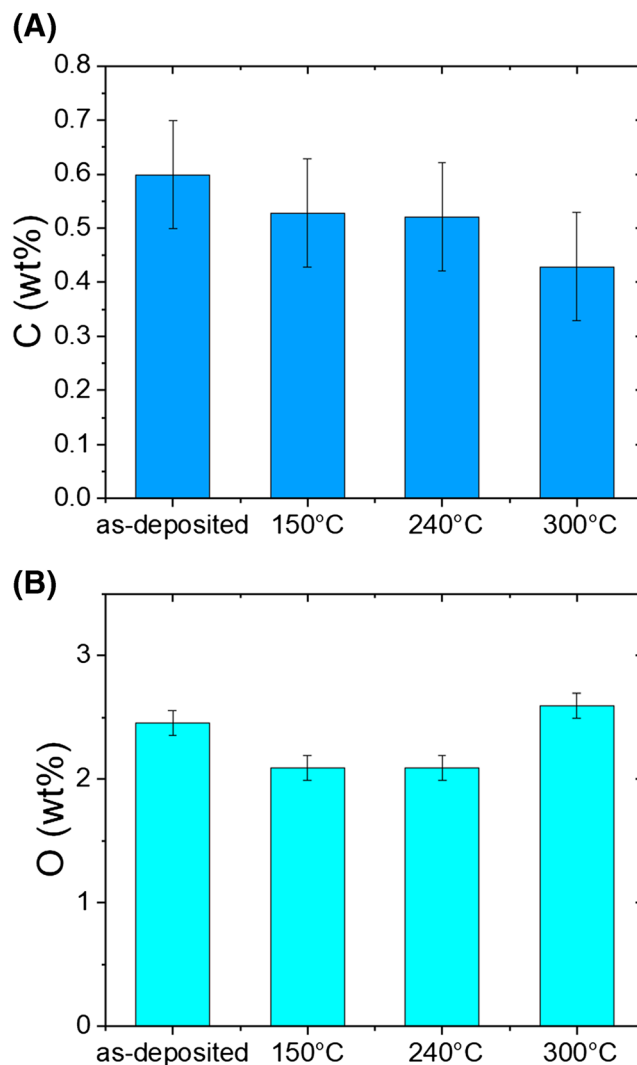


**FIGURE 8** (A) Carbon concentration and (B) oxygen content in Fe-C coatings as deposited and after annealing up to 300°C.

Results from the various spectroscopic methods suggest that the electrodeposited Fe-C coatings consist of different phases that contain carbon: (i) an organic phase in form of acetate; (ii) an amorphous carbon phase, also including hydrogenated carbon atoms; and (iii) a carbide phase, which formed in addition to carbon-free ferrite.

Very specific for the electrodeposited Fe-C coatings is the detection of iron acetate (cf. Figures 2B, 3, and 4), which contains the various codeposited nonmetallic elements (C, O, and H) that originate from the citric acid in the electrolyte. In as-deposited coatings, acetate seems to be the dominant carbon-containing phase. Iron acetates are reported to decompose during annealing and depending on heating rate (e.g., at about 280°C for a heating rate of 2 K/min<sup>23</sup>), which is associated with the release of H<sub>2</sub>O and CO<sub>2</sub>.<sup>23–25</sup> Indeed, previous thermogravimetric analysis with combined mass spectroscopy for electrodeposited Fe-C coatings revealed a considerable desorption of CO<sub>2</sub> above 250°C.<sup>5</sup> Decomposition of acetate allows for the subsequent formation of precipitates containing the desorbed elements.<sup>23,24</sup> Indeed, previous in situ synchrotron X-ray diffraction during isochronal annealing of

electrodeposited Fe-C coatings revealed the formation of magnetite  $\text{Fe}_3\text{O}_4$  and cementite  $\text{Fe}_3\text{C}$  at temperatures of 259°C to 325°C and 310°C to 338°C, respectively, with the temperature spreads corresponding to the applied heating rate (2–8 K/min).<sup>5,6</sup> In the present study, no magnetite was observed in the coating annealed at 300°C, although the acetate phase has partially decomposed. It is likely that magnetite would form in our samples, which are isothermally annealed, at an annealing temperature higher than 300°C and/or after holding longer time at 300°C (regarding carbide formation, see below). Despite the obvious relation between the  $\text{CO}_2$  evolution<sup>5</sup> during annealing in an inert atmosphere and the subsequent precipitation of magnetite and cementite,<sup>5,6</sup> the former observations in literature can be explained only based on the present study that identified iron acetate in as-deposited coatings. Although acetate is not expected to have a huge impact on the mechanical properties of as-deposited coatings, its decomposition and the resulting formation of fine and uniformly dispersed precipitates is of essential importance for the reported hardness increase of annealed Fe-C coatings.<sup>4–6</sup>

In addition to acetate, also iron carbides are identified in the electrodeposited Fe-C coatings. Although suggested in previous studies despite obvious limits of experimental verification,<sup>3–6</sup> a real proof for the presence of carbides in as-deposited Fe-C coatings is obtained with the present study (cf. Figures 2A and 3). It is remarkable that the carbides and the amorphous carbon are well dispersed within the Fe-C coating (see ToF-SIMS depth profiles in Figure 4) that mainly consists of nanocrystalline ferrite. This can be considered a nanocomposite. This provides some similarity to coatings prepared by magnetron sputtering from pure graphite and pure Fe,<sup>17</sup> where amorphous carbon (a-C) is observed together with (sub)stoichiometric carbide phases ( $\text{FeC}_y$ ) of either amorphous or crystalline nature. Despite much higher carbon concentrations in Furlan et al.,<sup>17</sup> the C1s spectrum (peak shape) obtained on a  $\text{Fe}_{1-x}\text{C}_x$  coating with 21 at.% C content<sup>17</sup> corresponds remarkably well with the C1s spectrum (peak shape) obtained for the present electrodeposited Fe-C coating (cf. Figure 3C). Furthermore, for the  $\text{Fe}_{1-x}\text{C}_x$  coating in Furlan et al.,<sup>17</sup> a distinct XRD peak evolves within a broad range of increased intensity indicating that the  $\text{FeC}_y$  carbides are not fully amorphous.<sup>17</sup> Interestingly, both the region of evolving peak intensity and the asymmetric peak shape in Furlan et al.<sup>17</sup> correspond well with the previously reported single peak observed by diffraction analysis of as-deposited Fe-C coatings<sup>4–6</sup> and termed “nameless phase,”<sup>3</sup> which disappears at temperatures above 328°C.<sup>5</sup> Despite the striking correlations, an unambiguous conclusion on the type of carbide in the present Fe-C coating cannot be obtained. The present results show a substoichiometric carbide phase ( $\text{FeC}_y$ ) of either amorphous or crystalline nature in the as-deposited coating. After partial decomposition of the acetate phase, the aforementioned carbide phase becomes the dominant carbon-containing phase in the Fe-C coating annealed at 300°C. Further decomposition of the acetate phase at higher temperatures would likely lead to the formation of cementite ( $\text{Fe}_3\text{C}$ ) precipitates.<sup>4–6</sup>

The detection of a-C or a-C:H is a noteworthy result from the present study. Although the fraction and the  $\text{sp}^2/\text{sp}^3$  ratio cannot be

quantified for the present coatings (cf. Figures 2C and 3 and Table 3), the results suggest a dominant  $\text{sp}^2$  character. Further investigations would be needed to understand the importance of this (minor) phase and its possible relation to either so-called diamond-like carbon or graphene, which so far are reported only for all-carbon coatings.

## 5 | CONCLUSION

Fe-C coatings were obtained by electrochemical deposition from an iron sulfate electrolyte with citric acid as carbon source. Motivated by the need to understand their previously reported excellent mechanical properties in relation to the high-carbon concentrations (0.6 wt.% C for the present samples), the nature of codeposited carbon and the resulting carbon-containing phases were investigated. To distinguish the carbon in the coatings from irrelevant surface contamination, isotopic citric acid resulting in  $^{13}\text{C}$  atoms was partly utilized. The applied analysis with complementary ToF-SIMS, XPS, and SXES using very carefully selected experimental conditions essentially enhanced the understanding of both as-deposited and annealed Fe-C coatings.

In addition to nanocrystalline ferrite, several carbon-containing phases are found in electrodeposited Fe-C coatings: (i) an organic phase in form of iron acetate, (ii) an amorphous carbon phase that also includes hydrogenated carbon atoms, and (iii) substoichiometric iron carbide ( $\text{FeC}_y$ ). They all are detected in both as-deposited and annealed Fe-C coatings up to 300°C, but their fraction changes during postdeposition annealing. The results clearly reveal that the electrochemical deposition of Fe-C coatings with intentionally codeposited carbon provokes unique phases in the coatings, which are distinct different to the ones in unalloyed steels despite the same carbon content. The citric acid in the electrolyte is crucial for the chemical and phase composition.

Of particular importance for the coatings' properties, and of essential difference to Fe-C coatings obtained by other than electrochemical deposition, is the formation of acetate. It explains not only the incorporation of carbon but also locates oxygen and hydrogen, which are known to be codeposited together with carbon and also provided by citric acid and corresponding reactions in the electrolyte. While acetate seems to be the dominant carbon-containing phase in as-deposited coatings, its decomposition during annealing is expected to facilitate the formation of magnetite and cementite precipitates.

The results indicate that the various carbon-containing phases are distributed homogeneously in the electrodeposited Fe-C coatings. In addition to the type and composition of these phases (with/without additional oxygen and hydrogen), the resulting nanocomposite consisting of the various phases embedded in ferrite is important for the well-known mechanical properties of both as-deposited and annealed Fe-C coatings.

## ACKNOWLEDGMENTS

The authors acknowledge Debora Rosseel (OCAS NV) and Kurt De Sloover (OCAS NV) for the sample preparation and TGA

measurements. The authors acknowledge Fonds Wetenschappelijk Onderzoek (FWO) for the funding of XPS research infrastructure (project number I006220N).

## CONFLICT OF INTEREST

The authors declare that they have no conflict of interests.

## DATA AVAILABILITY STATEMENT

The data that support the findings of this study are available from the corresponding author upon reasonable request.

## ORCID

Kristof Marcoen  <https://orcid.org/0000-0003-2831-483X>

## REFERENCES

- Fujiwara Y, Izaki M, Enomoto H, Nagayama T, Yamauchi E, Nakae A. Optimization of bath composition for hard Fe-C alloy plating. *J Appl Electrochem*. 1998;28(8):855-862. doi:[10.1023/A:1003444610964](https://doi.org/10.1023/A:1003444610964)
- Müller T, Grimwood J, Bachmaier A, Pippan R. Electrodeposition of Fe-C alloys from citrate baths: structure, mechanical properties, and thermal stability. *Metals (Basel)*. 2018;8(5):363-375. doi:[10.3390/met8050363](https://doi.org/10.3390/met8050363)
- Nielsen JO, Møller P, Pantleon K. Electrodeposition of iron with co-deposition of carbon - on the nature of nanocrystalline Fe-C coatings. *Met Mater Trans a*. 2019;50A:3785-3793.
- Nielsen JO, Pantleon K. Evolution of hard Fe-C electrodeposits with temperature. *Surf Eng*. 2020;36(9):960-965. doi:[10.1080/02670844.2019.1675305](https://doi.org/10.1080/02670844.2019.1675305)
- Nielsen JO, Christiansen TL, Pantleon K. In-situ analysis of the thermal evolution of electrodeposited Fe-C coatings. *Met Mater Trans a*. 2020;51A:4880-4889.
- Nielsen JO, Grummen FB, Pantleon K. Thermal evolution of ferrite in electrodeposited iron-carbon coatings in relation to phase transformations during post-deposition annealing. *Mater Charact*. 2021;172:110886.
- Erard GAE, Nielsen JO, Pantleon K. Repair of damaged surfaces with hard iron-carbon coatings. *Surf Eng*. 2022;38(1):56-61. doi:[10.1080/02670844.2022.2028059](https://doi.org/10.1080/02670844.2022.2028059)
- Izaki M. Electrodeposition of iron and iron alloys. In: Schlesinger M, Paunovic M, eds. *Modern Electroplating*. 5th ed. John Wiley & Sons; 2010.
- Mulone A, Nicolenco A, Hoffmann V, Klement U, Tsyntsa N, Cesiulis H. In-depth characterization of as-deposited and annealed Fe-W coatings electrodeposited from glycolate-citrate plating bath. *Electrochim Acta*. 2018;261:167-177. doi:[10.1016/j.electacta.2017.12.051](https://doi.org/10.1016/j.electacta.2017.12.051)
- Izaki M, Omi T. Structural characterization of martensitic iron-carbon alloy films electrodeposited from an iron(II) sulfate solution. *Met Mater Trans A*. 1996;27A(2):483-486. doi:[10.1007/BF02648429](https://doi.org/10.1007/BF02648429)
- Fujiwara Y, Nagayama T, Nakae A, Izaki M, Enomoto H, Yamauchi E. Electrodeposition of Fe-C alloys from baths containing dicarboxylic acids with a linear alkyl chain. *J Electrochem Soc*. 1996;143(8):2584-2590. doi:[10.1149/1.1837051](https://doi.org/10.1149/1.1837051)
- Haseeb ASMA, Hayashi Y, Masuda M, Arita M. On the nature of the electrochemically synthesized hard Fe-0.96 mass pct C alloy film. *Met Mater Trans B*. 2002;33B(6):921-927.
- Fukumuro N, Kojima S, Fujino M, et al. Hydrogen-induced superabundant vacancies in electroplated Fe-C alloy films. *J Alloys Compd*. 2015;645:404-407.
- Danilov FI, Protsenko VS, Ubiikon AV. Kinetic regularities governing the reaction of electrodeposition of iron from solutions of citrate complexes of iron(III). *Russ J Electrochem*. 2005;41(12):1282-1289. doi:[10.1007/s11175-005-0216-7](https://doi.org/10.1007/s11175-005-0216-7)
- Terauchi M, Kawana M. Soft-X-ray emission spectroscopy based on TEM—toward a total electronic structure analysis. *Ultramicroscopy*. 2006;106(11-12):1069-1075.
- Terauchi M, Koshiya S, Satoh F, et al. Chemical state information of bulk specimens obtained by SEM-based soft-X-ray emission spectrometry. *Microsc Microanal*. 2014;20(3):692-697. doi:[10.1017/S1431927614000439](https://doi.org/10.1017/S1431927614000439)
- Furlan A, Jansson U, Lu J, Hultman L, Magnuson M. Structure and bonding in amorphous iron carbide thin films. *J Phys Condens Matter*. 2015;27(4):045002. doi:[10.1088/0953-8984/27/4/045002](https://doi.org/10.1088/0953-8984/27/4/045002)
- Lascovich JC, Giorgi R, Scaglione S. Evaluation of the sp<sup>2</sup>/sp<sup>3</sup> ratio in amorphous carbon structure by XPS and XAES. *Appl Surf Sci*. 1991;47(1):17-21. doi:[10.1016/0169-4332\(91\)90098-5](https://doi.org/10.1016/0169-4332(91)90098-5)
- Kaciulis S. Spectroscopy of carbon: from diamond to nitride films. *Surf Interface Anal*. 2012;44(8):1155-1161. doi:[10.1002/sia.4892](https://doi.org/10.1002/sia.4892)
- Watts JF, Leadley SR, Castle JE, Blomfield CJ. Adsorption of PMMA on oxidized Al and Si substrates: an investigation by high-resolution X-ray photoelectron spectroscopy. *Langmuir*. 2000;16(5):2292-2300. doi:[10.1021/la981558b](https://doi.org/10.1021/la981558b)
- Morgan DJ. Comments on the XPS analysis of carbon materials. *J Carbon Res*. 2021;7(3):51. doi:[10.3390/c7030051](https://doi.org/10.3390/c7030051)
- McKenzie DR. Tetrahedral bonding in amorphous carbon. *Rep Prog Phys*. 1996;59(12):1611-1664. doi:[10.1088/0034-4885/59/12/002](https://doi.org/10.1088/0034-4885/59/12/002)
- Oliveira de Souza A, Biondo V, Ivashita FF, Colombelli de Souza Nunes G, Paesano A Jr. Structural and magnetic characterization of nanostructured iron acetate. *Orbital Electron J Chem*. 2017;9(4):261-265.
- Jewur SS, Kuriacose JC. Studies on the thermal decomposition of ferric acetate. *Thermochim Acta*. 1977;19(2):195-200. doi:[10.1016/0040-6031\(77\)85107-1](https://doi.org/10.1016/0040-6031(77)85107-1)
- Langbein H, Michalk C, Knese K, Eichhorn P. Thermal decomposition of freeze-dried complex acetates of iron, nickel and zinc, and structural characterisation of products. *J Eur Ceram Soc*. 1991;8(3):171-176. doi:[10.1016/0955-2219\(91\)90071-7](https://doi.org/10.1016/0955-2219(91)90071-7)

## SUPPORTING INFORMATION

Additional supporting information can be found online in the Supporting Information section at the end of this article.

**How to cite this article:** Marcoen K, Gauvin M, De Cleene A, et al. Identification of carbon-containing phases in electrodeposited hard Fe-C coatings with intentionally codeposited carbon. *Surf Interface Anal*. 2023;1-11. doi:[10.1002/sia.7196](https://doi.org/10.1002/sia.7196)